Materials Advances

ROYAL SOCIETY OF CHEMISTRY

PAPER

View Article Online
View Journal | View Issue

Cite this: *Mater. Adv.*, 2024, 5, 6255

Upcycling waste plastic into 2D-carbon nanomaterials for high-performance supercapacitors by incorporating $NiCo_2O_4$: a sustainable approach to renewable energy

Diksha Bhatt,[a] Mayank Pathak,[a] Nishtha Thakur,[b] Gaurav Tatrari,[a] Tanmoy Rath,[c] Zaher Judeh [b] and Nanda Gopal Sahoo *[a]

Received 5th May 2024,
Accepted 25th June 2024

DOI: 10.1039/d4ma00469h

rsc.li/materials-advances

A two-step catalytic pyrolysis technique is utilized to produce reduced graphene oxide (rGO) from waste plastic and a hydrothermal synthetic route to produce $NiCo_2O_4$ nanorods and $NiCo_2O_4$@WPrGO nanocomposites. The waste plastic derived reduced graphene oxide (WPrGO) provided the conductive network and stimulated the growth of $NiCo_2O_4$ nanorods on its surface in order to increase the collection and transportation of electrons during electrochemical charge storage performance. This technique makes $NiCo_2O_4$@WPrGO suitable for supercapacitor electrode materials. The electrochemical properties of the composites were evaluated using both two and three-electrode systems in 2 M KOH solution. The outstanding specific capacitance values of the $NiCo_2O_4$@WPrGO material and its symmetric prototype cell from CV and GCD were around 1566 F g^{-1} and 400 F g^{-1} (at scan rate of 2 mV s^{-1}) and 1105 F g^{-1} and 334 F g^{-1} (at current density of 0.5 A g^{-1}), respectively, with 2 M KOH electrolyte. Moreover, the assembled symmetric and asymmetric cell delivers high energy densities of 17 W h kg^{-1} and 45.08 W h kg^{-1} at the power densities of 153 W kg^{-1} and 980 W kg^{-1} respectively, along with high cycling stability of 86% and 88.5% after 15 000 and 3000 cycles, respectively.

1. Introduction

Currently, fossil fuels are the primary source of energy production and consumption accounting for more than 80% of the energy requirements.[1] The Global Energy Report predicts that by 2050, the world's energy demand will reach approximately 27.6 TW.[2] However, the swift depletion of natural fuel reserves has resulted in an insufficiency in meeting the escalating energy demands, leading to possible imminent and severe energy crises.[3,4] Moreover, the escalating global human population and the ongoing advancements in industrialization have had detrimental impacts on the environment and the availability of non-renewable fossil fuel energy sources.[5,6] This has posed a significant challenge, prompting widespread attention and a concerted focus on the exploration, development, and utilization of clean, sustainable, and renewable energy resources and their associated technologies.[7,8]

In this context, supercapacitors (SCs)/ultra-capacitors are a promising energy storage technology that has the potential to displace batteries and other traditional energy storage systems because of their high power/energy density, excellent reliability, rapid charge/discharge rate, long life cycle stability (>100 000 cycles), low maintenance and environmental friendliness.[9–11] However, the substantial impediments of high costs and low energy density in supercapacitors (SCs) persist as significant challenges in emerging applications such as electric vehicles (EVs), renewable energy storage systems, and next-generation electronic systems.[12] Consequently, extensive research efforts have been undertaken to surmount this obstacle and enhance the energy density of supercapacitors, aiming to rival or exceed that of batteries. This involves the exploration of new active electrode materials and innovative electrolytes characterized by affordability, compatibility, and a broad operating voltage range.[13,14] The three primary types of electrode materials employed in supercapacitor electrodes are conductive porous carbonaceous materials, transition metal oxides, and conductive polymers. The carbonaceous materials such as activated carbon, carbon fibers, carbon nanotubes (CNTs), graphene, graphene oxide, and reduced graphene oxide are electric double-layer capacitor (EDLC) active electrode materials that store electrical energy through the electrostatic adsorption of

[a] *PRS-NSNT Centre, Department of Chemistry, D.S.B. Campus, Kumaun University, Nainital, Uttarakhand-263002, India. E-mail: ngsahoo@yahoo.co.in*
[b] *School of Chemistry, Chemical Engineering and Biotechnology, Nanyang Technological University, Singapore*
[c] *Motihari College of Engineering (Bihar Engineering University), Department of Applied Sciences, Motihari, Bihar-845401, India*

charges at the electrode–electrolyte interface. On the other hand, transition metal oxides/sulfides[15]/hydroxides and conductive polymers are pseudocapacitive materials that exhibit higher specific capacitance and hold the potential to achieve battery-level energy density while retaining the life cycle and power density of EDLCs[16,17] and store charge *via* fast reversible faradaic charge transfer between the electrode–electrolyte interfaces.[18–20] Recently, zinc-iodine battery-capacitors and metal-ion capacitors efficiently combine carbon-based electrochemical double-layer capacitors with battery/pseudocapacitor electrode materials through the use of charge carriers such as Li^+, K^+, Na^+, Mg^{2+}, Ca^{2+}, NH^{4+}, and Zn^{2+}. With this combination, the energy density constraints of traditional aqueous supercapacitors are overcome by improving specific capacitance and widening the operating voltage.[21–23] By using substituted perovskite material as the positive electrode material in hybrid supercapacitors, one can further increase the energy density of a supercapacitor.[24,25]

Graphene, a flat monolayer of all-sp^2-hybridized carbon atoms closely packed into a two-dimensional (2D) honeycomb lattice, has rapidly emerged as an intriguing unique material among all carbonaceous materials. Graphene is anticipated to be an excellent material for energy conversion and storage applications such as solar cells, fuel cells, and supercapacitors owing to its fascinating properties, including tunable band gap, extraordinary electronic transport properties, excellent thermal conductivity, great mechanical strength ($\sim$1 TPa), good chemical stability, and exceptionally large surface area.[26,27]

Despite the advantages highlighted for graphene in supercapacitors, including its superior properties in various applications, its cost remains prohibitively high in the global market. In 2020, the worldwide cost of graphene in the international market amounted to USD 71.0 million. Projections indicate an anticipated increase to USD 785.2 million by 2028, representing a compound annual growth rate (CAGR) of 35.0% during the period spanning 2021 to 2028.[28] Graphene can be synthesized using a variety of methods, including graphite exfoliation, chemical vapor deposition (CVD) on metal surfaces, chemical coupling reactions, graphene oxide reduction, *etc.* However, large-scale production of graphene nanosheets remains a challenge due to time-consuming synthesis processes and cost-benefit constraints. Hence, in recent decades, alternative carbon-containing precursor materials for graphene synthesis have been widely investigated to ensure low cost and high yield preparation.[29–31]

Recently, waste plastics with high carbon content have garnered considerable attention for synthesizing graphene-based materials. Over the last decade, solid plastic waste has evolved into a globally significant environmental challenge due to its pervasive nature and resistance to biodegradation, particularly as it breaks down into nano and microplastic fragments, posing severe threats to living organisms and ecosystems. Given its affordability, plastic has become a widely utilized material, notably in the packaging industry, contributing significantly to municipal waste. Globally, 19–23 million metric tons of improperly managed plastic waste find their way from land-based sources to water bodies each year.[32,33] Therefore, it is imperative to discover and develop sustainable, cost-effective, and environmentally friendly methods to transform plastic waste into value-added products such as carbon nanomaterials, applicable across various industries. This approach not only addresses the pressing global challenge of plastic waste management, but also opens up a novel avenue for reclaiming value-added materials from plastic waste.[31,34] Achieving this goal involves the utilization of the modified pyrolysis technique (MPA), which converts waste plastic into valuable end products.

Single-layer graphene theoretically shows a specific capacitance of $\sim$21 uF cm^{-2} but if the entire surface area of graphene (2630 m^2 g^{-1}) is used, it can provide a huge specific capacitance of about 550 F g^{-1}.[35] However, due to unavoidable agglomeration or restacking of graphene nanosheets caused by strong intersheet van der Waals interaction during both the preparation and application processes, the practical capacitive behavior of pure graphene is lower than the expected value. As a result, the intrinsic capacitance of a single graphene sheet does not reflect as predicted, leading to significant degradation of the distinct properties of individual sheets, such as high specific surface area and electronic transport properties.[36–38] Therefore, the hybridization of graphene-based materials with redox-active materials improves the electrochemical performance of graphene-based supercapacitors and introduces spacers between graphene sheets to inhibit their aggregation, thus boosting the accessible surface area and promoting electrolyte ion diffusion.[39,40] Among all the various transition metal oxides, ternary nickel cobaltite ($NiCo_2O_4$) has drawn a lot of interest due to its excellent electrochemical performance, including superior electrical conductivity and significantly better electrochemical activity as a result of multiple redox reactions from both the Co^{3+}/Co^{2+} and Ni^{3+}/Ni^{2+} redox pairs present in $NiCo_2O_4$, leading to its high theoretical capacitance.[24,41] However, some drawbacks of $NiCo_2O_4$ restrict its broad-scale applications in supercapacitors such as its inherently poor electrical conductivity, which only permits a limited proportion of the active materials for redox reactions.[42] As a solution to this issue, composites of $NiCo_2O_4$ metal oxide with conductive carbonaceous nanomaterials have been widely explored for energy storage applications. Graphene-based materials owing to their splendid properties are an ideal choice among the various conductive carbon nanomaterials for acting as a carbon support for loading nanoparticles.[43,44] Therefore, it is possible to significantly increase the electrical conductivity by synthesizing a composite of $NiCo_2O_4$ and graphene-based materials. The collapse of graphene-based materials can also be avoided.[45]

Herein, we report a novel approach for the mass-scale synthesis of reduced graphene oxide (rGO) from solid waste plastic utilizing the pyrolysis technique. This approach addresses the critical issue of plastic waste while developing value-added graphene-based products in an economical and environmentally friendly manner. We also report the synthesis of $NiCo_2O_4$ nanorods and their composite with waste plastic-derived rGO ($NiCo_2O_4$@WPrGO) *via* a facile hydrothermal

method. The synthesized composite material was used as an active electrode material for supercapacitor cells, where its supercapacitive behavior with 2 M KOH electrolyte was investigated. The advancement of $NiCo_2O_4$-doped graphene-based electrodes presents a viable approach to augment energy storage technologies, thereby making a substantial contribution towards fulfilling the global energy requirements. Our approach is innovative since it addresses energy storage and waste management solutions simultaneously. Our study provides a solution to two major global concerns by turning waste plastics into high value rGO and creating sophisticated composite materials for supercapacitors. In addition to offering a practical plan for lowering plastic pollution, this creative method advances the research and development of sustainable energy storage.

To sum up, our research presents a technique for producing rGO in large quantities from waste plastic and illustrates the use of $NiCo_2O_4$@WPrGO composites in supercapacitor technology. This integrated strategy emphasizes the possibility of turning waste materials into useful resources, supporting energy innovation and environmental sustainability at the same time.

2. Experimental

2.1. Materials

For the synthesis of rGO, waste plastic as a precursor material was collected from the local municipality of Nainital, Uttarakhand, India. All chemicals, such as nickel nitrate hexahydrate, 98% [$Ni(NO_3)_2{\cdot}6H_2O$], cobalt nitrate hexahydrate, 99% [$Co(NO_3)_2{\cdot}6H_2O$], urea, 99% [CH_4N_2O], potassium hydroxide (KOH), *N*-methyl-2-pyrrolidone, 99.5% (NMP), polyvinylidene fluoride (PVDF), ethanol, graphite sheets (GSs), Whatman filter paper and bentonite clay, were used as received without further purification.

2.2. Synthesis of rGO from plastic waste (WPrGO)

By following the previously reported method by our research team, rGO was synthesized from waste plastics using an upcycling procedure albeit with some modifications to the experimental parameters that were made to tailor the material properties of rGO for SC applications.[46] Briefly, waste plastic as a precursor material was collected from the local municipality and flea market. The collected waste plastic is placed inside the shredder unit where it is chopped into fine pieces. The finely chopped plastics were then deeply washed with a soap solution in the washing unit to remove all the impurities, followed by drying inside the drying chamber. The shredded plastic was thoroughly integrated with bentonite nanoclay (a degradation catalyst) inside the mixing chamber in a specific weight percentage (0.5%). After this, the catalyst-mixed plastic sample underwent a two-stage pyrolysis process. In the first stage, the sample mixture was placed inside the primary pyrolysis reactor under an inert atmosphere of N_2 at 450 °C with a 5 °C minute^{-1} heating rate for the next 1 hour. As a result of this pyrolysis, all the petroleum products were removed and only carbon black residue was left inside the reactor. In the second stage, the black carbon residue obtained from the primary reactor was further processed inside a secondary pyrolysis reactor at 950 °C in a N_2 inert atmosphere with a heating rate of 10 °C minute^{-1} for the next 2 hours to obtain the final product, *i.e.*, WPrGO. The resulting product was then ball-milled for 10 hours, then repeatedly washed with 5% HCL solution and with double-distilled water to remove all impurities. The final product was obtained after a few hours of oven drying at 80 °C.

2.3. Synthesis of $NiCo_2O_4$ nanorods

For the synthesis of $NiCo_2O_4$ nanorods, 5 mM of $Ni(NO_3)_2{\cdot}6H_2O$ and 10 mM of $Co(NO_3)_2{\cdot}6H_2O$ (molar ratio 1 : 2) were mixed in 40 ml of double-distilled water (DDW) followed by gradual addition of 20 mM of urea under continuous stirring (Fig. 1). The mixture was stirred for another 30 min at room temperature until a homogeneous light pink colored solution is obtained. The solution mixture was then transferred to a 50 ml Teflon lined autoclave and heated at 140 °C for 12 h. The obtained precipitate was then collected, filtered, and washed with DDW and ethanol several times and then vacuum dried at 60 °C for 12 h. The dried sample was annealed at 400 °C for 3 h at a 10 °C min^{-1} heating rate.

2.4. Synthesis of the $NiCo_2O_4$@WPrGO composite

For the preparation of the $NiCo_2O_4$@WPrGO composite (Fig. 1), two solutions have been prepared and named sol. A and sol. B. For sol. A, 5 mM of $Ni(NO_3)_2{\cdot}6H_2O$ and 10 mM of $Co(NO_3)_2{\cdot}6H_2O$ were added in 30 ml of distilled water followed by slow addition of 20 mM of urea under stirring. The solution mixture is continuously stirred magnetically until the precursors are dissolved to give a homogenous pink color solution. On the other hand, for sol. B, 60 mg of waste plastic derived rGO (WPrGO) powder was added to 20 ml of DDW and stirred for 30 min. For better dispersion, this solution is subjected to a sonicator where high-energy sound waves uniformly disperse the particles of WPrGO into DDW. For maximum and better dispersion, this sonicated solution was further placed in an ultrasonic homogenizer for the next 30 minutes. Sol. A is now mixed with sol. B to give solution C, which was stirred continuously for 1 h. Sol. C was then treated in an intense ultrasonic homogenizer for the next 1 h at high power. The ultrasonic homogenizer disrupts the WPrGO layers through cavitation, with the ultrasonic waves resulting in more uniform mixing of the rGO matrix and metal oxide. The obtained homogeneous solution mixture was then transferred to a 50 ml Teflon-lined autoclave for the hydrothermal reaction at 140 °C for 12 h. The obtained precipitate was then collected, filtered, and washed with ethanol and DDW and then vacuum dried at 60 °C for 12 h. The dried sample was annealed at 400 °C for 3 h with a heating rate of 10 °C min^{-1} to give the final composite material.

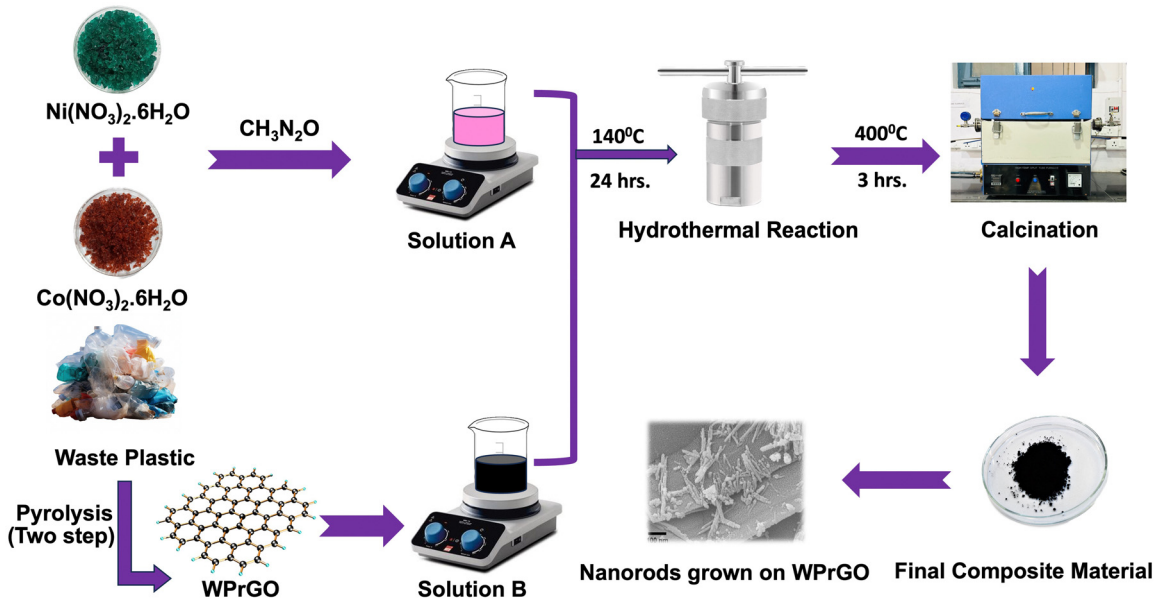

Fig. 1 Schematic representation of the synthesis of the $NiCo_2O_4$@WPrGO composite material.

2.5. Electrode and cell fabrication

To evaluate the electrochemical performance of the synthesized materials, an electrochemical test was performed *via* a two- and three-electrode system with 2 M KOH electrolyte. For the three-electrode system, the reference electrode was an Ag/AgCl electrode, and the counter electrode was a Pt wire. The working electrode was prepared by making a slurry of as-synthesized material by using polyvinylidene fluoride (PVDF) as a binder. Briefly, 5 wt% PVDF powder was dissolved in *N*-methylpyrrolidone (NMP) with continuous stirring until a homogenous solution was obtained. Then, 95 wt% synthesized material powder is mixed properly with 5 wt% PVDF solution using a mortar and pestle to obtain a slurry. Then, the prepared slurry of about 1 mg was coated over graphite sheets (GS) of 1 × 1 cm^2 area and then these electrodes were placed in an oven overnight at 80 °C.

For the two-electrode system, a prototype supercapacitor cell was fabricated. For the construction of the prototype cell, two electrodes made of graphite sheets with a surface area of 1 × 1 cm^2 were coated with a slurry of synthesized materials as prepared above, and a piece of Whatman filter paper (WFP) serving as a separator is then dipped into the electrolyte solution and sandwiched between the two electrodes. The working electrode thickness was estimated to be around 4.42 μm, based on graphite density (2.26 g cm^{-3}). These synthesized electrodes were dried overnight in an oven set to 80 °C.

3. Results and discussion

$NiCo_2O_4$@WPrGO was synthesized using a basic hydrothermal method and subsequent annealing. In this process, positively charged metal ions (Ni^{2+} and Co^{2+}) interacted electrostatically with the negatively charged reduced graphene oxide made from plastic waste. *In situ* hydrolysis of urea gradually released hydroxyl ions (OH^-) throughout the hydrothermal process.[44] These hydroxyl ions reacted with the Ni^{2+} and Co^{2+} metal ions to generate metal hydroxide nanoparticles [$Ni(OH)_2$ and $Co(OH)_2$]. Simultaneously, the slow hydrolysis of urea resulted in the production of CO_3^{2-} ions in the aqueous environment, which were believed to be significant in the formation of a one-dimensional nanorod structure. Metal hydroxyl carbonate complexes were then formed as a result of the metal hydroxides' interaction with the carbonate ions.[47] These metal hydroxyl carbonates underwent breakdown during the calcination procedure, resulting in the production of $NiCo_2O_4$ nanorods. The mechanism of this process is shown in Fig. 1. These nanorods were evenly distributed on sheets of reduced graphene oxide produced from plastic waste. During the synthesis procedure of the composite materials, the hydrolysis and decomposition reactions can be formulated broadly as:

$$NH_2CONH_2 \rightarrow NH_4^+ + NCO^-$$

$$NCO^- + 3H_2O \rightarrow HCO_3^- + NH_4^+ + OH^-$$

$$HCO_3^- \rightarrow CO_3^{2-} + H^+$$

$$Ni^{2+} + 2Co^{2+} + 3OH^- + 1.5CO_3^{2-} \rightarrow NiCo_2(CO_3)_{1.5}(OH)_3$$

$$NiCo_2(CO_3)_{1.5}(OH)_3 + \frac{1}{2}O_2 \rightarrow NiCo_2O_4 + 1.5H_2O + 1.5CO_2$$

3.1. Structural and morphological characterization of WPrGO, $NiCo_2O_4$ and $NiCo_2O_4$@WPrGO

Raman and TGA. Raman spectroscopy is a widely used advanced characterization technique for the identification of graphene-based materials. The result has been discussed in our

previous research article.[11] The Raman spectrum of the synthesized WPrGO revealed the characteristic D and G bands at 1346 cm^{-1} (bond stretching of sp^3) and 1593 cm^{-1} (bond stretching of sp^2), respectively. The G band is also associated with the ordered E_{2g} vibrational mode of sp^2 hybridized carbon atoms which is used to assess the degree of graphitization. On the other hand, the D band is ascribed to the partially disordered sp^2 bonded carbon atom structure and used to depict the extent of structural defects of graphene. Furthermore, the peak intensity ratio of the G and D bands, *i.e.*, the I_G/I_D ratio is a measure of structural defects in graphene sheets. This ratio was found to be 0.84, which indicates some defects in the WPrGO structure.[44–46,48] Besides, a broad 2D band shifted to a higher wavenumber was seen at 2945.73 cm^{-1}.[49,50] The I_{2D}/I_G ratio for the sample was found to be ~0.45 which is significant to calculate the number of layers in the prepared WPrGO sample and indicates the synthesis of WPrGO. Thus, the presence of three characteristic bands, D, G and 2D confirmed the synthesis of WPrGO.

Thermogravimetric analysis (TGA) was carried out to assess the thermal stability, volatile group fraction of $NiCo_2O_4$@WPrGO and graphitic nature of WPrGO while monitoring weight loss (Fig. 2(a)). The weight loss in the WPrGO material up to 450 °C was caused by loss of intercalated water molecules between WPrGO layers. The second stage large weight loss in the temperature range of 450 °C to 690 °C is attributed to the elimination of oxygenated functional groups contained in the WPrGO material.[11] Conversely, weight loss in the $NiCo_2O_4$@WPrGO nanocomposite material up to 510 °C was attributed to the removal of moisture from the composite material, whereas the primary cause of weight loss in the temperature range of 510 °C to 775 °C is thought to be the breakdown of $NiCo_2O_4$ into NiO and Co_2O_3.

XRD and FT-IR. The FT-IR spectrum of WPrGO (Fig. 2(b)) showed different oxygenated and deoxygenated peaks at 1047 cm^{-1}, 1343 cm^{-1}, 1744 cm^{-1}, and 2331 cm^{-1} which are attributed to stretching vibration of the C–O epoxide bond, bending vibration of the C–OH bond, stretching vibration of the C═O bond of a carbonyl group and bending vibration of the CO_2 molecule, respectively. These FT-IR peaks of different functional groups support the synthesis and structure of WPrGO.

The FT-IR spectrum of $NiCo_2O_4$ (Fig. 2(b)) showed peaks at 2981 cm^{-1}, 2668 cm^{-1}, 2325 cm^{-1}, 1657 cm^{-1}, 1338 cm^{-1}, 636 cm^{-1} and 527 cm^{-1}. The peaks at 2981 cm^{-1}, 2668 cm^{-1}, and 2325 cm^{-1} are ascribed to the vibration of CO_2 by personal or environmental factors, and the peaks observed at 1657 cm^{-1} and 1338 cm^{-1} are assigned to the stretching vibration of atmospheric water absorbed by the sample. The two low frequency strong peaks at 642 cm^{-1} and 538 cm^{-1} correspond to stretching vibrations of the Ni–O and Co–O bonds in $NiCo_2O_4$. These two low-frequency peaks are the characteristic peaks that support the successful synthesis of $NiCo_2O_4$.[28,51]

The FT-IR spectrum of $NiCo_2O_4$@WPrGO (Fig. 2(b)) showed peaks at 2662 cm^{-1}, 2337 cm^{-1}, 1623 cm^{-1}, 1744 cm^{-1}, 1343 cm^{-1}, 1012 cm^{-1}, 630 cm^{-1} and 533 cm^{-1}. This spectrum showed peaks of both synthesized WPrGO and $NiCo_2O_4$, thus supporting the synthesis of the $NiCo_2O_4$@WPrGO composite. The peaks observed at 1744 cm^{-1}, 1343 cm^{-1}, and 1012 cm^{-1} were assigned to stretching vibration of the C═O bond of a carbonyl group, and bending vibration of the C–OH bond and C–O bond, respectively, which are also shown in the spectrum of WPrGO. But here the peak's intensity decreases, which indicates greater bonding interaction between such groups, as the weaker the bond, the greater the interaction.[45] On the other hand, the peaks at 2662 cm^{-1} and 2337 cm^{-1}, are ascribed to vibration of CO_2 due to personal or environmental factors, while the peaks at 630 cm^{-1} and 533 cm^{-1} are assigned to stretching vibrations of the Ni–O and Co–O bonds, which are characteristic peaks of $NiCo_2O_4$. Overall, this spectrum showed peaks of both WPrGO and $NiCo_2O_4$ and support the synthesis of the $NiCo_2O_4$@WPrGO composite.

The XRD analysis of WPrGO showed two diffraction peaks at 2θ = 26.65° (002 plane) and 42.45° (001) which correspond to a characteristic and graphitic peak of reduced graphene oxide. The XRD spectrum of both $NiCo_2O_4$ and $NiCo_2O_4$@WPrGO showed diffraction peaks at 2θ = 18.9°, 31.1°, 36.7°, 44.6°, 59.1° and 65.1°, corresponding to the (111), (220), (311), (400), (511) and (440) planes of $NiCo_2O_4$ (JCPDS No. 20-0781). The typical XRD spectrum of $NiCo_2O_4$@WPrGO also showed two wide and weak peaks at 2θ = 24.65° and 42.45°, which correspond to WPrGO and further support the synthesis of $NiCo_2O_4$@WPrGO. The combined XRD and FT-IR data of

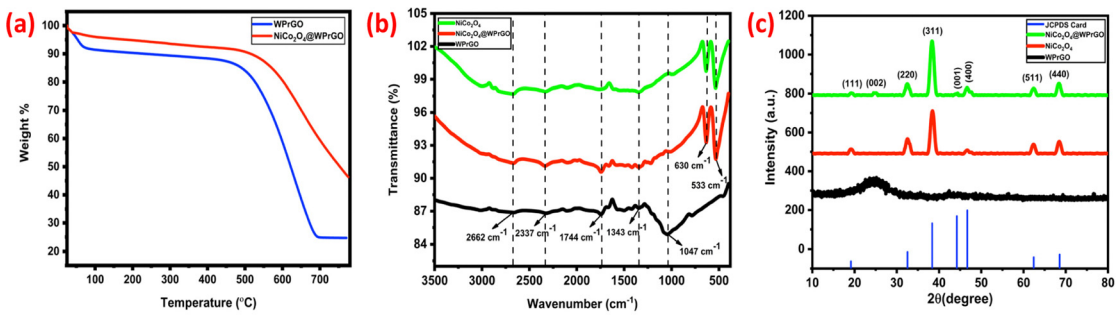

Fig. 2 TGA curve of WPrGO and $NiCo_2O_4$@WPrGO (a); FT-IR spectra of WPrGO, $NiCo_2O_4$, and $NiCo_2O_4$@WPrGO (b); XRD spectra of WPrGO, pure $NiCo_2O_4$, and $NiCo_2O_4$@WPrGO (c).

WPrGO, $NiCo_2O_4$ and $NiCo_2O_4$@WPrGO are shown in Fig. 2(a) and (b).

SEM/EDX, TEM, and XPS. SEM was performed to examine the surface morphology of the synthesized WPrGO, $NiCo_2O_4$, and $NiCo_2O_4$@WPrGO composite. The SEM image of WPrGO (Fig. 3(a) and (b)) reveals a sheet-like structure and it is seen as a multilayer, which may be due to the presence of oxidative sites above, below, and at the margin of the WPrGO sheets. The bright particles seen in the WPrGO SEM image can result from the aggregation of graphene oxide sheets or clusters during the reduction process. Agglomeration happens when discrete sheets or clusters of graphene oxide come into close contact with one another and are bound together by different factors like van der Waals forces and π–π stacking interaction. In the case of energy storage devices like supercapacitors, this agglomeration of rGO flakes limits ion diffusion and reduces the surface area, making it more difficult for electrical current to flow through them. As a result, it requires quick attention. A viable solution to this problem is to use conducting polymers, like polypyrrole (PPY) and polyaniline (PANI), redox-active nickel ferricyanide, carbon nanotubes, carbon black, and transition-metal oxides, like $NiCo_2O_4$, MoO_3, TiO_2, *etc.*, as a nanospacer between the rGO flakes to stop them from restacking and enhance the functionality of the devices. In our work, we add $NiCo_2O_4$ to the surface of WPrGO, which greatly enhances its suitability for use in supercapacitors.[52–54]

The SEM images of $NiCo_2O_4$ (Fig. 3(c) and (d)) at different magnifications show porous nanorod like structures which are densely packed and interconnected with each other. The SEM image of the $NiCo_2O_4$@WPrGO composite material shown in Fig. 3(e) and (f) reflects the growth of $NiCo_2O_4$ nanorods on WPrGO sheets vertically, which represents the excellent interaction between nickel cobaltite and WPrGO. Thus, based on SEM analysis, we further confirm the synthesis of WPrGO, $NiCo_2O_4$, and the $NiCo_2O_4$@WPrGO composite material.

Furthermore, the SEM data are supported by TEM images, which depict the internal morphology of the synthesized materials. The TEM image of WPrGO showed a sheet-like structure internally as also shown in the SEM image.[11] In brief, the TEM result indicates that WPrGO is internally separated as layers with some defective sites. The TEM image of pure $NiCo_2O_4$ (Fig. 4(a) and (b)) shows an agglomeration of nanorod-like structures, which are highly porous. On the other hand, the TEM image of the $NiCo_2O_4$@WPrGO (Fig. 4(c) and (d)) composite material showed the presence of a nanorod-like structure of $NiCo_2O_4$ over the thin and folded sheet-like structure of WPrGO, which confirms the successful incorporation of $NiCo_2O_4$. The diffused SAED pattern (Fig. 4(e)) at 5.1 nm of the $NiCo_2O_4$@WPrGO nanocomposite shows well-defined diffused rings, which indicate the nanocrystalline structure of $NiCo_2O_4$.

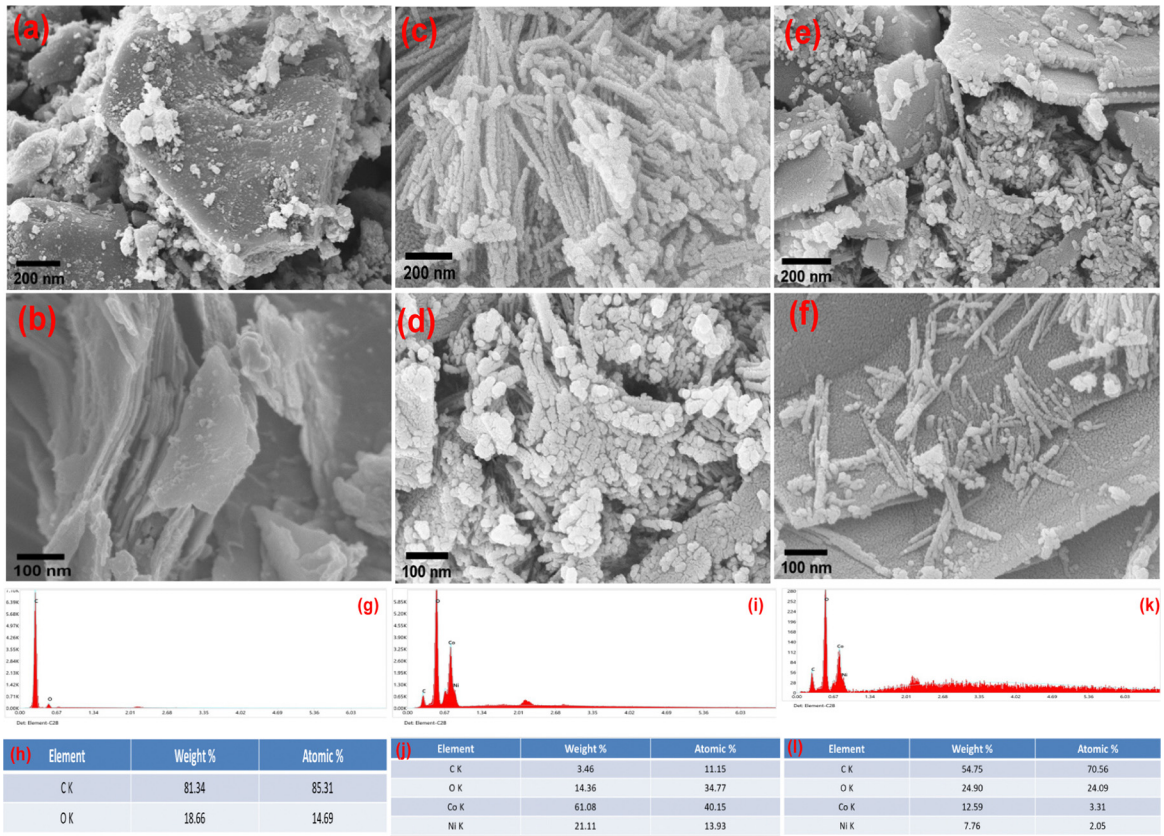

(h)

Element	Weight %	Atomic %
C K	81.34	85.31
O K	18.66	14.69

(j)

Element	Weight %	Atomic %
C K	3.46	11.15
O K	14.36	34.77
Co K	61.08	40.15
Ni K	21.11	13.93

(l)

Element	Weight %	Atomic %
C K	54.75	70.56
O K	24.90	24.09
Co K	12.59	3.31
Ni K	7.76	2.05

Fig. 3 SEM images of WPrGO, $NiCo_2O_4$ and $NiCo_2O_4$@WPrGO at 200 and 100 nm magnification (a)–(f); EDX spectrum and elemental composition table of WPrGO (g) and (h), $NiCo_2O_4$ (i) and (j) and $NiCo_2O_4$@WPrGO (k) and (l).

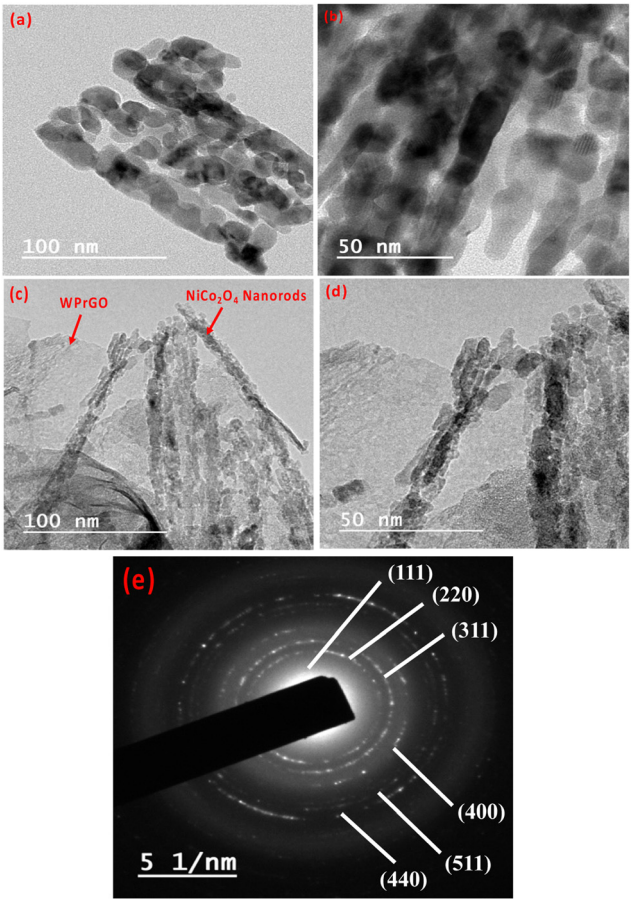

Fig. 4 TEM images of $NiCo_2O_4$ at 100 and 50 nm magnifications (a) and (b); TEM images of $NiCo_2O_4$@WPrGO at 100 and 50 nm magnifications (c) and (d); and SAED pattern of $NiCo_2O_4$@WPrGO (e).

Additionally, the EDX data, which was employed to assess the elemental composition in the samples, supported the SEM and TEM data. The EDX spectrum of the $NiCo_2O_4$@WPrGO composite material showed the existence of carbon (C), oxygen (O), nickel (Ni), and cobalt (Co) in the composite material in appropriate amounts. From the EDX spectrum, the atomic ratio of nickel (Ni) and cobalt (Co) was found to be 1 : 2, which confirms the synthesis of $NiCo_2O_4$.

The elemental compositions as well as the chemical and electronic state of the atoms within the $NiCo_2O_4$@WPrGO composite material were analyzed by performing X-ray photoelectron spectroscopy (XPS). The presence of C, O, Ni, and Co elements within the $NiCo_2O_4$@WPrGO material was depicted in the survey spectrum (Fig. 5(a)). In Fig. 5(b), the high-resolution XPS spectrum of C 1s has been deconvoluted into four Gaussian curves centered at 284.6 eV, 286.1 eV, 287.7 eV, and 288.5 eV, attributed to C–C, C–O, C═O and O═C–O groups, respectively.[10,45] The intensity of the peaks for the oxygen-related groups diminished greatly, which indicates the reduction of GO into rGO and doping of heteroatoms.[47] As shown in Fig. 5(e), the O 1s emission spectrum has two deconvoluted peaks at 528.9 eV and 529.0 eV. The peak at 528.9 eV was attributed to the metal-oxygen bond (Ni–O or Co–O or Ni–O–Co bond) and the peak at 530.9 eV was assigned to surface-adsorbed hydroxyl groups and oxygen elements.[55]

In Fig. 5(d), the Ni 2p XPS spectrum depicts two characteristic spin–orbit doublets of Ni^{2+} and Ni^{3+} and two broad shakeup satellites. The energy peaks at 854.2 eV and 872.5 eV are assigned to Ni^{2+}, while the other peaks at 855.8 eV and 871.7 eV correspond to Ni^{3+}. On the contrary, the Co 2p spectrum (Fig. 5(c)) also shows two double peaks attributed to Co^{2+} and Co^{3+} ions. The doublet peaks at 780.2 eV and 795.3 eV were assigned to Co^{2+}, while another doublet peak at 779.2 eV and 794.3 eV belongs to Co^{3+}. Thus, the Ni 2p and Co 2p spectra demonstrate the presence of $Co^{3+/2+}$ and $Ni^{3+/2+}$ coupled ions on the surface of the $NiCo_2O_4$@WPrGO composite material.

3.2. Electrochemical performance of the synthesized samples

Cyclic voltammetry (CV), chronopotentiometry (CP), and electrochemical impedance spectroscopy (EIS) methods were used to assess the electrochemical properties of the freshly synthesized materials. A three-electrode setup was used for these studies, with a 2 M KOH aqueous solution serving as the electrolyte. The active material, a platinum wire, and an Ag/AgCl electrode, respectively, serve as the working, counter, and reference electrodes in this configuration.

The working electrode was made by coating a graphite sheet (1×1 cm^2) with a combination of 95% prepared materials and 5% polyvinylidene fluoride (PVDF), which was then dried at 80 °C. The mass of the active substance in the electrode was around 1 mg. The symmetric supercapacitor prototype cell with a $NiCo_2O_4$@WPrGO electrode was subjected to electrochemical experiments using a two-electrode setup. Cyclic voltammetry (CV) measurement was performed to investigate the electrochemical characteristics of the electrode material over an optimized voltage range. The following equation may be used to compute the specific capacitance from CV curves:

$$C_s = \frac{A}{2mKV} \quad (1)$$

In the above formula, C_s represents the specific capacitance, A is the integrated surface area that the CV curve covers, m denotes the mass of electrode material coated on the current collector (in mg), K indicates the scan rate (in mV s^{-1}), and V represents the voltage difference between the CV curves.

Additionally, GCD tests were carried out at varying current densities across fixed voltage ranges to assess the charging–discharging performance and the cycling stability of the as-prepared materials and constructed supercapacitor cells. The following equation may be used to determine the specific capacitance based on the charge/discharge test:

$$C_s = \frac{I\Delta t}{m\Delta V} \quad (2)$$

where m indicates the mass of electrode material coated on the current collectors in mg, Δt denotes the discharging period in seconds, and ΔV stands for the potential window.

The two key factors that define the performance of the SCs are energy and power density. How much energy a gadget holds

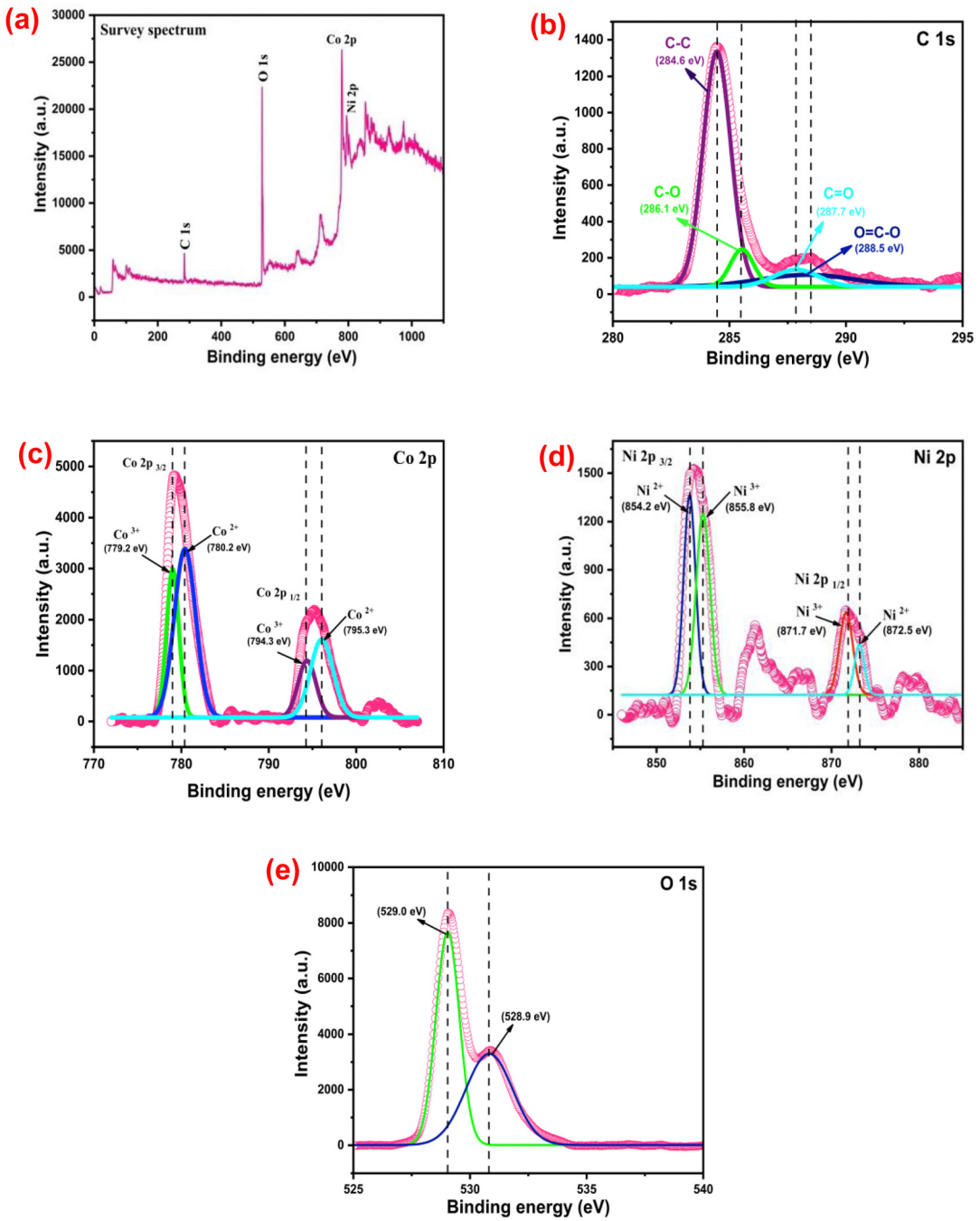

Fig. 5 XPS spectra of $NiCo_2O_4$@WPrGO; survey spectra (a), C 1s (b), Co 2p (c), Ni 2p (d) and O 1s (e).

is referred to as the energy density. The following formula was used to get the energy density:

$$ED = \frac{0.5 \times C(\Delta V)^2}{3.6} \quad (3)$$

where ΔV denotes the potential window and C denotes the specific capacitance at a certain current density.

How rapidly a device can discharge its energy is referred to as the SC's power density. The following formula was used to determine the power density (PD) of the constructed gadget.

$$PD = \frac{ED \times 3600}{\Delta t} \quad (4)$$

ED is the energy density of the device at a particular current density, and Δt is the discharging time duration.

The coulombic efficiency (η) of the charge storage process gauges how simple it is to introduce and remove ions throughout the charging and discharging operations. With the aid of the formula, the manufactured prototype supercapacitor cell's

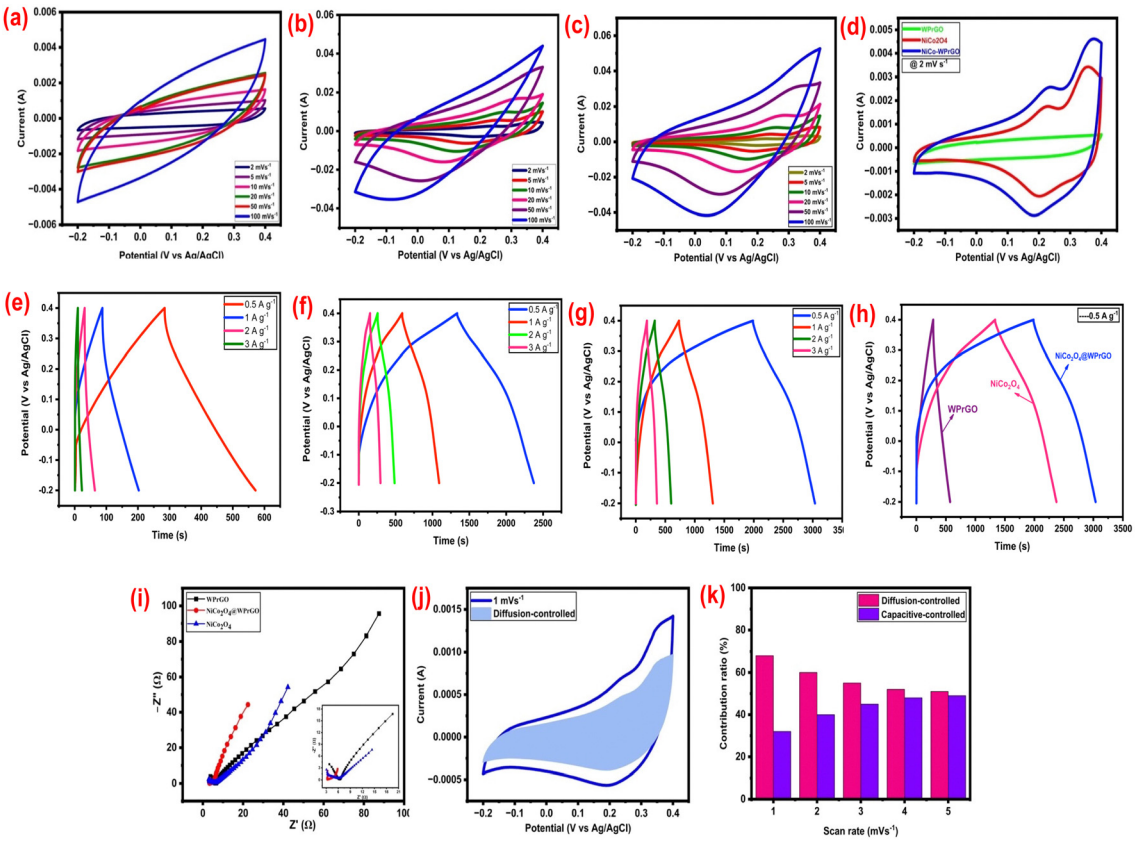

Fig. 6 Electrochemical characterization of the as-obtained materials in 2 M KOH aqueous electrolyte with a three-electrode setup: CV curves of WPrGO, $NiCo_2O_4$ and $NiCo_2O_4$@WPrGO at various scan rates (a)–(c), and combined CV curves at 2 mV s^{-1} (d). Chronopotentiometry plots of WPrGO, $NiCo_2O_4$ and $NiCo_2O_4$@WPrGO at various scan rates (e)–(g), and combined GCD curves at 0.5 A g^{-1} (h). A combined Nyquist plot for WPrGO, $NiCo_2O_4$ and $NiCo_2O_4$@WPrGO in a frequency range of 1 MHz to 10 mHz (i), with an inset plot of magnified view. A CV curve of the composite material at 1 mV s^{-1} differentiated into diffusion and surface capacitance (j) and the contribution ratio at various scan rates (k).

coulombic efficiency (%) was determined.

$$\eta = \frac{t_c}{t_d} \times 100 \quad (5)$$

where t_c and t_d denote the charging and discharging time, respectively.

A three-electrode electrochemical cell utilizing a 2 M KOH aqueous solution as the electrolyte was employed to assess the spectacular electrochemical performance of the produced material electrodes with enhanced specific energy for supercapacitor applications. The cyclic voltammetry (CV) curves for WPrGO, $NiCo_2O_4$, and $NiCo_2O_4$@WPrGO in the potential range of −0.2 to 0.4 V (total voltage 0.6) are shown in Fig. 6(a)–(c) at different scan rates of 2, 5, 10, 20, 50, and 100 mV s^{-1}.

The specific capacitance (C_s) of $NiCo_2O_4$@WPrGO was measured at various scan rates: 2, 5, 10, 20, 50, and 100 mV s^{-1}, yielding values of around 1566, 1240, 978, 766, 568, and 390 F g^{-1}, respectively. The aforementioned values were much greater than the specific capacitance of pure $NiCo_2O_4$ (1054, 1002, 873, 751, 470, and 262 F g^{-1} at 2, 5, 10, 20, and 50 mV s^{-1}, respectively) and WPrGO (336, 220, 160, 114, 72, and 47 F g^{-1} at 2, 5, 10, 20, and 50 mV s^{-1}, respectively). This highlights $NiCo_2O_4$@WPrGO's potential for enhanced supercapacitor performance by demonstrating a significant improvement in the specific capacitance compared to the individual components.

Fig. 6(d) shows the cyclic voltammetry (CV) curves of WPrGO, $NiCo_2O_4$, and $NiCo_2O_4$@WPrGO, all recorded at a scan rate of 2 mV s^{-1} for comparison purposes (the mass of all the loaded electrode materials was the same). The WPrGO CV curves are typically not ideal, but rather nearly rectangular with a small deviation caused by electrode resistance, such as ion transfer resistance, electrode material resistance, or even some surface redox related to oxygen functional groups, particularly at high scan rates.[56] Capacitive currents at the electrode–electrolyte interface cause the CV curve to diverge from the ideal rectangular shape connected to only faradaic processes, resulting in curved features or a leaf-like shape. The electrochemical behaviour of rGO can also be affected by residual oxygen-containing functional groups present on its surface. Non-rectangular CV peaks may result from these functional groups interacting with electrolyte ions or going through redox processes.[57] In contrast, both pure $NiCo_2O_4$ and $NiCo_2O_4$@WPrGO demonstrate distinct and well-defined reversible redox peaks. These peaks can be attributed to the

M–O/M–O–OH (where M stands for Co and Ni ions) faradaic redox processes taking place in the KOH electrolyte. A charge storage mechanism may explain this behavior using the mechanisms listed below.[58–60]

$$NiCo_2O_4 + OH^- + H_2O \rightarrow NiOOH + 2CoOOH + e^-$$

$$CoOOH + OH^- \rightarrow CoO_2 + H_2O + e^-$$

The current range and the area enclosed by the CV curve have a direct effect on a material's specific capacitance. It is clear from Fig. 6(d) that, at the same scan rate (2 mV s^{-1}), the current range and the region underneath the CV curve for $NiCo_2O_4$@WPrGO are much bigger than those of pure $NiCo_2O_4$ and WPrGO. This distinct difference illustrates the enhanced capacitance performance of the $NiCo_2O_4$@WPrGO composite electrode as compared to its individual components. The higher capacitive performance of $NiCo_2O_4$@WPrGO can be ascribed to better charge transfer made possible by the high electrical conductivity of reduced graphene oxide made from plastic waste. The specific capacitance for $NiCo_2O_4$@WPrGO, pure $NiCo_2O_4$, and WPrGO electrodes at a scan rate of 2 mV s^{-1} is determined using the cyclic voltammetry formula (as shown in eqn (1)) to be around 1566 F g^{-1}, 1054 F g^{-1}, and 336 F g^{-1}, respectively. A combination of these results and CV plots indicates that the $NiCo_2O_4$@WPrGO composite material has the best capacitive performance, making it a good candidate for use in supercapacitors.

Chronopotentiometry investigations were carried out at several current densities, including 0.5 A g^{-1}, 1 A g^{-1}, 2 A g^{-1}, and 3 A g^{-1}, within a potential range of −0.2 to 0.4 V (total voltage 0.6), to offer a more thorough knowledge of the supercapacitive behaviour of the manufactured electrode. Fig. 6(e)–(g) shows galvanostatic charge–discharge (GCD) profiles for WPrGO, $NiCo_2O_4$, and $NiCo_2O_4$@WPrGO at various current densities, while maintaining a constant potential of 0.6 V. $NiCo_2O_4$@WPrGO's specific capacitance (C_s) was calculated by applying eqn (2) to be around 1105 F g^{-1}, 965 F g^{-1}, 931 F g^{-1}, and 858 F g^{-1} at 0.5 A g^{-1}, 1 A g^{-1}, 2 A g^{-1}, and 3 A g^{-1}, respectively. These figures substantially surpass the specific capacitance of WPrGO (245 F g^{-1}, 192 F g^{-1}, 108 F g^{-1}, and 65 F g^{-1} at 0.5 A g^{-1}, 1 A g^{-1}, 2 A g^{-1}, and 3 A g^{-1}, respectively) and pure $NiCo_2O_4$ (865 F g^{-1}, 839 F g^{-1}, 772 F g^{-1}, and 708 F g^{-1}), at the corresponding current densities. It's important to understand that the decreased capacitance reported at greater current densities is caused by the ions' slower diffusion and migration through the electrode–electrolyte contact. Conversely, the maximum capacitance values at lower current densities refer to effective diffusion and quick ion transport across the electrode–electrolyte interface.[61]

Fig. 6(h) provides a comprehensive comparison of the galvanostatic charge–discharge curves for the WPrGO, $NiCo_2O_4$, and $NiCo_2O_4$WPrGO electrodes, which were measured at a current density of 0.5 A g^{-1}. Calculations revealed that the $NiCo_2O_4$@WPrGO, $NiCo_2O_4$, and WPrGO electrodes each had a specific capacitance of around 1105 F g^{-1}, 865 F g^{-1}, and 245 F g^{-1}, respectively. Notably, the $NiCo_2O_4$@WPrGO electrode surpasses both the $NiCo_2O_4$ and WPrGO electrodes in terms of capacitive performance, showing the greatest specific capacitance.

The equivalent sheet resistance (ESR) or the internal resistance of the material was assessed by performing electrochemical impedance spectroscopy (EIS) in a frequency range of 10 mHz to 10^6 Hz, which was shown using the Nyquist plot. The Nyquist plot depicts the relationship between the fictitious component ($-Z''$) and the actual component (Z') of the impedance, expressed in ohms. This plot provides insights into the impedance characteristics of the material. In the supercapacitor performance of the samples, the EIS findings highlighted two distinct frequency zones. These regions, which encompass both high and low frequencies, relate to different resistance phenomena that take place throughout the electrochemical processes.[62] A noticeable increase in the lower frequency range of the Nyquist plot indicates the material's capacitive behavior. On the other hand, the existence of a semicircular zone in the higher frequency region indicates the system's bulk resistance, which results from the charge transfer resistance that takes place between the electrode and electrolyte interface. The Nyquist plot often shows a semicircle and a straight line joined at a 90-degree angle. The charge transfer resistance (R_{ct}) between the electrode and the electrolyte is represented by this semicircle.

It can be seen in Fig. 6(i) that the semicircular region inside the plot is relatively small, presumably due to the electrolyte's low faradaic resistance. In the inset of Fig. 6(i), the high frequency area is shown in greater detail. This makes the real axis intercept more easily visible and makes it possible to calculate the equivalent series resistance (ESR, R_s) value.

The Nyquist plot revealed that the ESR values of WPrGO, $NiCo_2O_4$, and $NiCo_2O_4$@WPrGO materials are, respectively, 3.7, 3.3, and 2.9 ohm. The high values of ESR of WPrGO and $NiCo_2O_4$ indicate that ion transport at the electrode–electrolyte interface is constrained. This may be explained as the main cause of the reduction in specific capacitance in WPrGO and $NiCo_2O_4$ when compared to $NiCo_2O_4$@WPrGO. The lower ESR value of the composite materials ($NiCo_2O_4$@WPrGO) results in improved electronic conditions and lower circuit impedance. In terms of stability, capacitance, and ion transportation around the interface of the electrolyte and electrode materials, this has an impact on the overall performance of the materials. The ESR values obtained by interpreting the Nyquist plot were further validated through the application of an equivalent circuit model. An equivalent circuit model effectively fits the electrochemical impedance spectroscopy (EIS) data. In this model, several components are considered: R_s stands for the equivalent series resistance and is related to the ionic conductivity of the electrolyte as well as the electronic conductivity of the electrodes and current collectors, R_{ct} which symbolizes charge transfer resistance is attributed to the electrolyte–electrode interface, W denotes the Warburg resistance, which develops as a result of the transport or diffusion of electrolyte ions during redox processes involving $NiCo_2O_4$ and CPE (constant

phase element) corresponds to the double-layer capacitance present in the system.[59,60,63] The Nyquist plot may be more easily interpreted and analyzed by taking these factors into account while modelling EIS data.

The outcomes of the electrochemical assessment of the three materials with a three-electrode setup undeniably show that the $NiCo_2O_4$@WPrGO composite material holds more potential than WPrGO and $NiCo_2O_4$ as a suitable electrode for supercapacitor applications.

To further study the energy storage process and to explain how a composite material behaves in terms of capacitance, Dunn's method has been applied. Surface capacitance and diffusion capacitance are two separate factors that contribute to a material's capacitance behavior. The electric double layer that forms at a material's surface is what causes surface capacitance, which is controlled by a faradaic process for storing charge. The current–voltage relationship is linear when considering electrochemical double layer (EDL) capacitance. However, when analyzing diffusion capacitance, electrolyte ions are introduced onto the electrode material, exhibiting a redox-like behavior akin to batteries. The response of the current to the voltage is nonlinear because of this diffusion capacitance.[10,64] The current in this scenario can be explained as follows:

$$i = k_1 v + k_2 v^{0.5} = i_c + i_d \quad (6)$$

where v is the scan rate (in mV s^{-1}), k_1 and k_2 are constants, and i is the current in A at a fixed voltage. In the equation above, the terms $k_1 v$ and $k_2 v^{0.5}$ stand for surface-controlled capacitance (also known as i_c) and diffusion-controlled capacitance (also known as i_d), respectively.

Furthermore, the values of the constants k_1 and k_2 can be easily computed as the slope and intercept, respectively, by plotting the $i/v^{0.5}$ *vs.* $v^{0.5}$ plot. Additionally, the composite material was examined using Dunn's method at a low scan rate of 1 mV s^{-1} to 10 mV s^{-1} with a potential window of −0.2 to 0.4 V. We specifically determined the current that resulted from the surface capacitance, or i_c, and the current that was produced by the diffusion capacitance, or i_d, at a scan rate of 1 mV s^{-1}. The diffusion-controlled capacitative contribution at a scan rate of 1 mV s^{-1}, which accounts for 68.4% of the total capacity, is represented by the shaded region in Fig. 6(j). We can observe the capacitive contributions at various scan rates in Fig. 6(k). The surface capacitive contribution eventually becomes more significant as the scan rate is increased from 1 to 5 mV s^{-1}. This information enables us to make the conclusion that at higher scan rates, the surface capacitance plays a more substantial role than the diffusion capacitance, and at lower scan rates, the diffusion capacitance becomes the dominating contributor.

A symmetric supercapacitor cell was meticulously assembled to see whether using $NiCo_2O_4$@WPrGO as an electrode material in supercapacitors is practically feasible. In this configuration, $NiCo_2O_4$@WPrGO was used as the electrode material, and electrochemical tests were then performed utilizing a 2 M KOH electrolyte. Fig. 7(a) shows the CV curves of the fabricated prototype cell of $NiCo_2O_4$@WPrGO measured at different scan rates from 2–100 mV s^{-1} in a potential range of 0 to 0.6 V. All CV curves exhibited a similar quasi rectangular shape even at a scan rate of 100 mV s^{-1}, which suggests that supercapacitor cells have a good rate capability. The specific capacitance (C_s) of the fabricated prototype cell at different scan rates of 2, 5, 10, 20, 50, and 100 mV s^{-1} was calculated from the corresponding CV curves and are found to be 400.2,

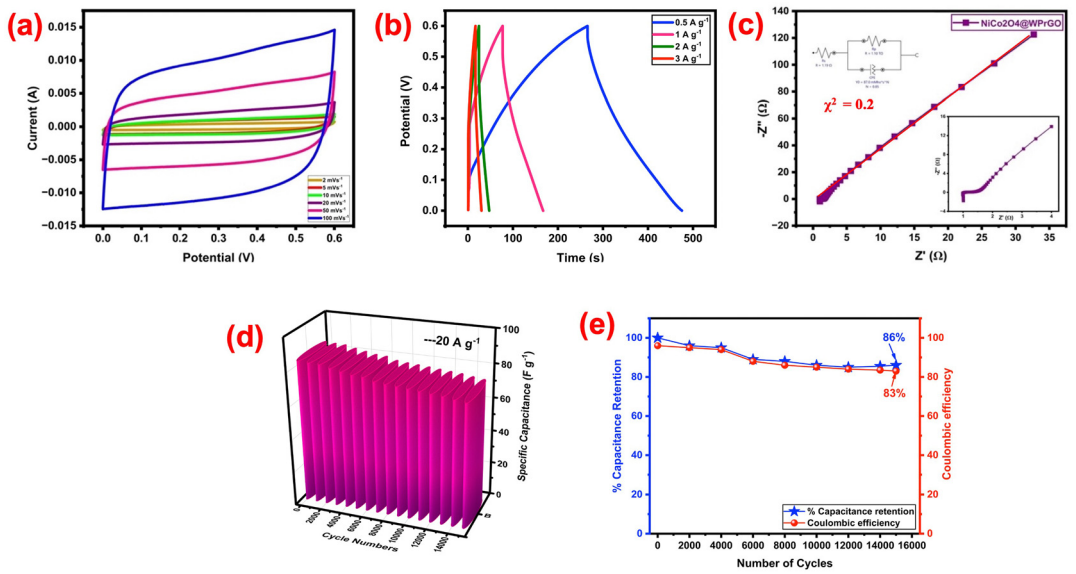

Fig. 7 Electrochemical characterization of the $NiCo_2O_4$@WPrGO symmetric cell in 2 M KOH aqueous electrolyte with a two-electrode setup: cyclic voltammogram curves at various scan rates (a); GCD curves at various current densities (b); Nyquist plot in the frequency range of 10 mHz to 10^6 Hz with an inset showing a magnified view (c). Cycling stability test in terms of specific capacitance value (d) and cycling stability test in terms of percentage capacitance retention with coulombic efficiency of the fabricated supercapacitor cell (e), both at 20 A g^{-1} current density.

345, 223, 214, 205 and 192 F g^{-1}, respectively. Additionally, the cell was subjected to galvanostatic charge–discharge experiments with current densities ranging from 0.5 A g^{-1} to 3 A g^{-1}. At varying current densities of 0.5, 1, 2, and 3 A g^{-1}, the cell's computed specific capacitances were found to be 334, 206, 154, and 143 F g^{-1}, respectively (Fig. 7(b)). The long-term cycling stability of the fabricated prototype cell was further tested by charge–discharge plot up to 15 000 cycles at 20 A g^{-1} over a wide potential range of 0 to 0.6 V displayed in Fig. 7(e). The device showed superior cycling stability with 86% of the initial specific capacitance retained after 15 000 cycles (Fig. 7(f)). This much capacitive retention of the $NiCo_2O_4$@WPrGO made cell may be attributed to the venerable interaction between metal oxide ions and WPrGO. In addition, the fabricated cell showed 83% coulombic efficiency.

Electrochemical impedance spectroscopy (EIS) study at a frequency range of 10 mHz to 10^6 Hz was also utilized to identify the equivalent sheet resistance (ESR) or cell internal resistance. As noted in Fig. 7(c), the plot has much less semicircular region, which may be a result of the electrolyte's poor faradaic resistance. The inset of Fig. 7(c), which provides a magnified view of the high frequency area, aids in visualizing the real axis intercept and the value of equivalent series resistance (ESR, R_s). The inset of Fig. 7(c) also provides the circuit fitting model. The accuracy of the circuit model was verified by chi square test. The degree of fitting between the measured EIS data and calculated results is evaluated by minimizing the chi-square statistic (χ^2). A chi-square value close or equal to 0 indicates that the model fits the data well.[65,66] In our analysis, the chi-square value was found to be 0.2 (Table 1), which is near to 0, confirming that the EIS fitting is accurate and reliable. In Fig. 7(c) the red line shows the perfect fitting of the circuit. This provides confidence in the validity of our impedance analysis and the selection of appropriate equivalent circuits to describe the electrochemical behaviour of the system. The fabricated cell's ESR value was discovered to be around 1 ohm. The low ESR value in a low frequency region demonstrates good supercapacitive performance and typical EDLC behavior of $NiCo_2O_4$@WPrGO as an electrode material for supercapacitors. The $NiCo_2O_4$@WPrGO material shows an excellent energy density of about 55 W h kg^{-1} at a power density of 153 W kg^{-1}.

For comparison purposes, the specific capacitance values obtained from the CV and GCD plots of $NiCo_2O_4$@WPrGO *via* two and three electrode systems are displayed in Table 1.

Table 1 Comparison of the specific capacitances of $NiCo_2O_4$@WPrGO based electrodes between two- and three-electrode systems using the following methods: CV at 5 mV s^{-1} scan rate, GCD at 0.5 A g^{-1} current density and EIS at 10 MHz frequency

Material	$NiCo_2O_4$@WPrGO based electrode	
Parameters	CV@2 mV s^{-1}	GCD@0.5 A g^{-1}
C_s from 2-electrode system	400.2 F g^{-1}	334 F g^{-1}
C_s from 3-electrode system	1546 F g^{-1}	1105 F g^{-1}

To investigate the capacitive performance of $NiCo_2O_4$@WPrGO in real-world applications, an asymmetric supercapacitor cell (ASC) was designed with $NiCo_2O_4$@WPrGO as the positive electrode and WPrGO as the negative electrode, denoted as $NiCo_2O_4$@WPrGO//WPrGO. Using $NiCo_2O_4$@WPrGO and WPrGO, the ASC cell's potential can be increased to 1.4 V. The following formula should be used to determine the mass ratio of the material that serves as the positive electrode to the negative electrode material.

$$\frac{m_+}{m_-} = \frac{C_- \times \Delta V_-}{C_+ \times \Delta V_+} \quad (7)$$

where m is the electrode material's loaded mass, ΔV is the voltage range, and C is the electrode material's specific capacitance. Given that the $NiCo_2O_4$@WPrGO composite and WPrGO electrodes have specific capacitances of 1105 F g^{-1} and 245 F g^{-1}, respectively, the ideal mass ratio between the two electrodes is $m_{(WPrGO)}/m_{(NiCo_2O_4@WPrGO)}$ = 2.5 in order to create an asymmetric supercapacitor. The $NiCo_2O_4$@WPrGO//WPrGO CV curves (Fig. 8(a)), which were obtained at a scan rate of 20 mV s^{-1} and with different working voltages ranging from 0.0–1.0 V to 0.0–1.4 V, show a stable potential window up to 1.4 V. The $NiCo_2O_4$@WPrGO//WPrGO galvanostatic charge–discharge curves at 1 A g^{-1} are displayed in Fig. 8(b); the symmetric charge–discharge curves highlight the ASC's good capacitive properties. Fig. 8(c) displays the $NiCo_2O_4$@WPrGO//WPrGO CV curves at potential ranges of 0–1.4 V recorded at different scan rates of 2–100 mV s^{-1}. The specific capacitances of the ASC were calculated to be 156.7, 138.2, 115.7, 97.7, 69.23, and 52.91 F g^{-1} at 2, 5, 10, 20, 50, and 100 mV s^{-1}. It appears that $NiCo_2O_4$@WPrGO//WPrGO had a decent rate capability because all of the CV curves showed a comparable shape even at a scan rate of 100 mV s^{-1}. Additionally, the ASC underwent galvanostatic charge–discharge testing at a range of current densities, from 1 A g^{-1} to 4 A g^{-1}. Based on the total mass of the electrode materials, the ASC's computed specific capacitances were 165.6, 58.8, 45.2, and 39.2 F g^{-1} at current densities of 1, 2, 3, and 4 A g^{-1}, respectively (Fig. 8(d)). To assess the cycling stability of the $NiCo_2O_4$@WPrGO//WPrGO, a charge–discharge cycling test was performed at a current density of 6 A g^{-1}. With 88.5% of the initial specific capacitance remaining after 3000 cycles, Fig. 8(e) demonstrates exceptional cyclic stability. The energy and power densities of the ASC were calculated using eqn (3) and (4). The $NiCo_2O_4$@WPrGO//WPrGO supercapacitor demonstrated a high energy density of 45.08 W h kg^{-1} and a power density of 980 W kg^{-1}.

From the above analysis, it is clearly observed that the $NiCo_2O_4$@WPrGO nanocomposites show enhanced supercapacitor performance as compared to the bare $NiCo_2O_4$ nanorods and WPrGO. Moreover, Table 2 illustrates how the $NiCo_2O_4$@WPrGO nanocomposites perform better than those from earlier published data. The $NiCo_2O_4$@WPrGO nanocomposites exhibit comparable specific capacitance values at lower current densities, capacitance retention, energy density, and power density to other materials under similar conditions of experimentation. More precisely, $NiCo_2O_4$@WPrGO

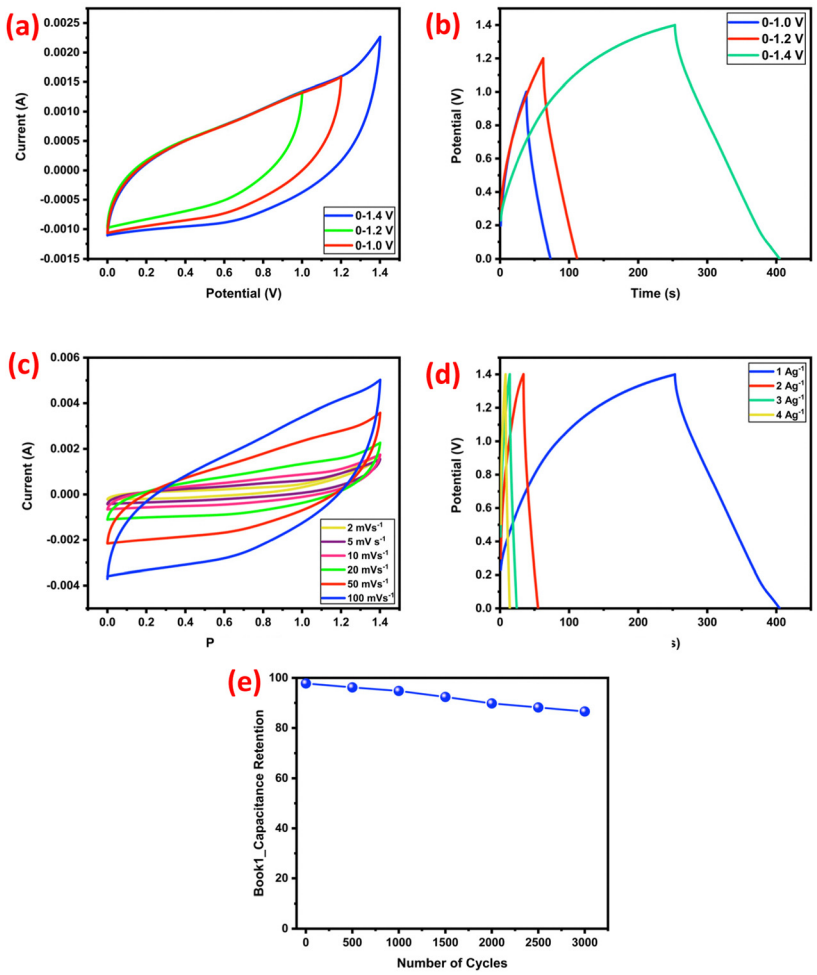

Fig. 8 Cyclic voltammogram curves of the asymmetric supercapacitor in a potential window from 1.0 to 1.4 V at a scan rate of 20 mV s^{-1} (a); GCD curves of the asymmetric supercapacitor in a potential window from 1.0 to 1.4 V at 1 A g^{-1} (b); cyclic voltammogram curves of the asymmetric supercapacitor at various scan rates (c); GCD curves of the asymmetric supercapacitor at various current densities (d); and charge–discharge cycling test of the asymmetric supercapacitor at the current density of 6 A g^{-1} (e).

Table 2 Comparison of the present work with previously reported work

S. no.	Material	Electrolyte	Specific capacitance (F g^{-1})	Current density (A g^{-1})	Capacitance retention after cycling stability	Energy density (W h Kg^{-1})	Power density (W Kg^{-1})	Ref.
1	$NiCo_2O_4$/rGO	2 M KOH	1757	1	90% after 10 000 cycles	32.38	797	33
2	Ni/Co-MOF-rGO	6 M KOH	860	1	91.6% after 6000 cycles	72.8	850	67
3	$NiCo_2O_4$/NF	1 M KOH	1076	0.5	86% after 500 cycles	30.5	750	68
4	$NiCo_2O_4$@MnO_2	1 M KOH	913.6	0.5	87.1% after 3000 cycles	37.5	7500	69
5	CNT/$NiCo_2O_4$	6 M KOH	695	1	91% after 1500 cycles	16.4	118.4	70
6	$NiCo_2O_4$/rGO/CF	3 M KOH	931.7	1	83.8% after 5000 cycles	24.6	850.3	71
7	$NiCo_2O_4$/GQDs	2 M KOH	667.6	1	99.4% after 5000 cycles	26.2	920.8	72
8	$NiCo_2O_4$-WPrGO	2 M KOH	1105	0.5	88.5% after 3000 cycles	45.08	980	This work

nanocomposites exhibit specific capacitance of 1105 F g^{-1} in 2 M KOH electrolyte, surpassing the specific capacitance values reported in the literature for $NiCo_2O_4$-based composite materials. This comparison demonstrates that $NiCo_2O_4$@WPrGO nanocomposites display exceptional electrochemical performance and underlines their potential for cutting-edge energy storage applications.

4. Conclusion

This article describes the modified and cost-effective, two-step pyrolysis method that was used to successfully produce reduced graphene oxide from solid waste plastic. This approach is environmentally friendly, recycling waste materials to create a valuable energy storage component. This approach not only

addresses the pressing global challenge of plastic waste management, but also opens up a novel avenue for reclaiming value-added materials from plastic waste. The use of $NiCo_2O_4$ as a component in the composite could offer advantages such as high capacitance, good electrical conductivity, and electrochemical stability. A bimetallic $NiCo_2O_4$ oxide was synthesized by means of a hydrothermal approach, followed by calcination at 400 °C for a duration of 3 hours. The hydrothermally formed $NiCo_2O_4$ bimetallic oxide had a nanorod-like structure and was integrated onto sheets of reduced graphene oxide, resulting in the development of the $NiCo_2O_4$@WPrGO composite material. Notably, the resultant $NiCo_2O_4$ nanoparticles were tightly bound to the porous layout of the reduced graphene oxide inside the $NiCo_2O_4$@WPrGO composite. The successful synthesis of WPrGO, $NiCo_2O_4$ bimetallic oxide with a nanorod like morphology and $NiCo_2O_4$@WPrGO composite material was confirmed by RAMAN spectroscopy, XRD analysis, TEM analysis, SEM analysis and FT-IR spectroscopy. Techniques including cyclic voltammetry (CV), galvanostatic charge–discharge (GCD), and electrochemical impedance spectroscopy (EIS) were used to assess the electrochemical properties of the synthesized materials. The outstanding specific capacitance values of the $NiCo_2O_4$@WPrGO material and its symmetric prototype cell were around 1105 F g^{-1} and 334 F g^{-1}, respectively with 2 M KOH electrolyte, when operating at a current density of 0.5 A g^{-1}. Furthermore, an asymmetric prototype cell denoted as $NiCo_2O_4$@WPrGO//WPrGO was fabricated with 2 M KOH electrolyte, and the specific capacitance of the ASC prototype cell was calculated around 165.6 F g^{-1} at a current density of 1 A g^{-1}. Additionally, the assembled symmetric and asymmetric cell had noteworthy energy density statistics, reaching 17 W h kg^{-1} and 45.08 W h kg^{-1}, respectively, along with power density values of 153 W kg^{-1} and 980 W kg^{-1}. Furthermore, the fabricated symmetric and asymmetric device showed excellent cycling stability with the specific capacitance retention of about 86% after 15 000 cycles and 88.5% after 3000 cycles. The remarkable capacitive performance will undoubtedly make the $NiCo_2O_4$@WPrGO material attractive for high performance electrode materials in energy storage applications.

Author contributions

Diksha Bhatt: conceptualization, methodology, experiments, investigation, writing complete draft; Mayank Pathak: review; Nishtha Thakur: characterization; Gaurav Tatrari: review, Tanmoy Rath: formal analysis, editing, grammar check; Zaher Judeh: formal analysis, grammar check; Nanda Gopal Sahoo: conceptualization, complete review and editing, and supervision.

Data availability

The datasets generated and analysed during the current study are not publicly available due to the ongoing research project, but are available from the corresponding author upon reasonable request.

Conflicts of interest

The authors declare no conflict of interest for the present work.

Acknowledgements

The authors would like to acknowledge the National Mission of Himalayan Studies (NMHS), Kosi Katarmal, India (Ref. No. NMHS/2022-23/MG 86/03/279) and School of Chemistry, Chemical Engineering and Biotechnology, Nanyang Technological University, Singapore for their financial support.

References

1 S. Yadav and A. Devi, *J. Energy Storage*, 2020, **30**, 101486.
2 S. J. Lee, J. Theerthagiri, N. Palaniyandy, P. Arunachalam, B. Dhandapani, M. K. Arumugam, J. Madhavan, V. Mittal and M. Y. Choi, *Renewable Sustainable Energy Rev.*, 2021, **143**, 110849.
3 P. Simon and Y. Gogotsi, *Nat. Mater.*, 2008, **7**, 845–854.
4 K. Li, C. Shan, S. Fu, H. Wu, W. He, J. Wang, L. Gui, Q. Mu, S. Du, Q. Zhao, C. Hu and H. Guo, *Energy Environ. Sci.*, 2024, **17**, 580–590.
5 M. S. Rahmanifar, H. Hesari, A. Noori, M. Y. Masoomi, A. Morsali and M. F. Mousavi, *Electrochim. Acta*, 2018, **275**, 76–86.
6 W. Utetiwabo, L. Yang, M. K. Tufail, L. Zhou, R. Chen, Y. Lian and W. Yang, *Chin. Chem. Lett.*, 2020, **31**, 1474–1489.
7 M. Sethi, U. S. Shenoy and D. K. Bhat, *J. Alloys Compd.*, 2021, **854**, 157190.
8 R. Liang, Y. Du, P. Xiao, J. Cheng, S. Yuan, Y. Chen, J. Yuan and J. Chen, *Nanomaterials*, 2021, **11**, 1248.
9 N. Alhokbany, J. Ahmed, M. Ubaidullah, S. Mutehri, M. A. M. Khan, T. Ahamad and S. M. Alshehri, *J. Mater. Sci.: Mater. Electron.*, 2020, **31**, 16701–16707.
10 Z. Shi, G. Sun, R. Yuan, W. Chen, Z. Wang, L. Zhang, K. Zhan, M. Zhu, J. Yang and B. Zhao, *J. Mater. Sci. Technol.*, 2022, **99**, 260–269.
11 M. Karakoti, S. Pandey, R. Jangra, P. S. Dhapola, P. K. Singh, S. Mahendia, A. Abbas and N. G. Sahoo, *Mater. Manuf. Processes*, 2020, **36**, 171–177.
12 M. Pathak, G. Tatrari, M. Karakoti, S. Pandey, P. S. Sahu, B. Saha and N. G. Sahoo, *J. Energy Storage*, 2022, **55**, 105729.
13 M. Pathak, D. Bhatt, R. Bhatt, B. S. Bohra, G. Tatrari, S. Rana, M. C. Arya and N. G. Sahoo, *Chem. Rec.*, 2024, **24**, e202300236.
14 L. L. Zhang, R. Zhou and X. Zhao, *J. Mater. Chem.*, 2010, **20**, 5983.
15 X. Liang, Y. Chen, Z. Jiao, M. Demir, M. Du and J. Han, *J. Energy Storage*, 2024, **88**, 111634.
16 P. Simon, Y. Gogotsi and B. Dunn, *Science*, 2014, **343**, 1210–1211.

17 P. Simon and Y. Gogotsi, *Nat. Mater.*, 2020, **19**, 1151–1163.
18 W. Shi, J. Zhu, D. Sim, Y. Y. Tay, Z. Lu, X. Zhang, Y. Sharma, M. Srinivasan, H. Zhang, H. H. Hng and Q. Yan, *J. Mater. Chem.*, 2011, **21**, 3422.
19 J. Barqi, S. M. Masoudpanah, M. Hasheminiasari and X. Liu, *J. Alloys Compd.*, 2023, **930**, 167509.
20 Y. A. Kumar and H.-J. Kim, *RSC Adv.*, 2019, **9**, 1115–1122.
21 Z. Sun, X. Han and D. Wang, *J. Energy Storage*, 2023, **62**, 106857.
22 D. Wang, J. Sun and L. Chen, *ChemSusChem*, 2023, **12**, 202300207.
23 D. Wang, X. Han and X. Zhang, *J. Power Sources*, 2024, **599**, 234215.
24 G. Liu, L. Liu, G. Li, S. Wu, J. He, Y. Zhou, M. Demir and P. Ma, *Chem. – Eur. J.*, 2024, 202303267.
25 Y. Qiao, J. He, Y. Zhou, S. Wu, X. Li, G. Jiang, M. Demir and P. Ma, *ACS Appl. Mater. Interfaces*, 2023, **45**, 52381–52391.
26 G. Ak and K. C. Novoselov, *Nat. Mater.*, 2007, **6**, 183–191.
27 A. Armano and S. Agnello, *C*, 2019, **5**, 67.
28 Zion Market Research. **https://www.zionmarketresearch.com/report/graphene-market**, 2021 (accessed 06 July, 2021).
29 G. Tatrari, M. Karakoti, C. Tewari, S. Pandey, B. S. Bohra, A. Dandapat and N. G. Sahoo, *Mater. Adv.*, 2021, **2**, 1454–1484.
30 K. R. Shamskar, A. Rashidi, P. A. Azar, M. Yousefi and S. Baniyaghoob, *Environ. Sci. Pollut. Res. Int.*, 2018, **26**, 3643–3650.
31 G. Tatrari, C. Tewari, B. S. Bohra, S. Pandey, M. Karakoti, S. Kumar, H. Tiwari, S. Dhali and N. G. Sahoo, *Cleaner Eng. Technol.*, 2021, **5**, 100275.
32 M. Bergmann, F. Collard, J. Fabrés, G. W. Gabrielsen, J. F. Provencher, C. M. Rochman, E. Van Sebille and M. B. Tekman, *Nat. Rev. Earth Environ.*, 2022, **3**, 323–337.
33 A. O. C. Iroegbu, S. S. Ray, V. Mbarane, J. Bordado and J. P. Sardinha, *ACS Omega*, 2021, **6**, 19343–19355.
34 S. Pandey, M. Karakoti, S. Dhali, N. Karki, B. SanthiBhushan, C. Tewari, S. Rana, A. Srivastava, A. B. Melkani and N. G. Sahoo, *Waste Manage.*, 2019, **88**, 48–55.
35 M. F. El-Kady, V. Strong, S. Dubin and R. B. Kaner, *Science*, 2012, **335**, 1326–1330.
36 K. Qin and J. Wang, *J. Materiomics*, 2016, **2**, 37–54.
37 Z. Fan, Q. Zhao, T. Li, J. Yan, Y. Ren, J. Feng and T. Wei, *Carbon*, 2012, **50**, 1699–1703.
38 K. Zhang, L. Zhang, X. Zhao and J. Wu, *Chem. Mater.*, 2010, **22**, 1392–1401.
39 Z. Shi, G. Sun, R. Yuan, W. Chen, Z. Wang, L. Zhang, K. Zhan, M. Zhu, J. Yang and B. Zhao, *J. Mater. Sci. Technol.*, 2022, **99**, 260–269.
40 H. Wang, Z. Hu, Y.-Q. Chang, Y. Chen, H. Wu, Z. Zhang and Y. Yang, *J. Mater. Chem.*, 2011, **21**, 10504.
41 Y. Lei, J. Li, Y. Wang, L. Gu, Y. Chang, H. Yuan and D. Xiao, *ACS Appl. Mater. Interfaces*, 2014, **6**, 1773–1780.
42 C. Zhang, X. Geng, S. Tang, M. Deng and Y. Du, *J. Mater. Chem. A*, 2017, **5**, 5912–5919.
43 Y. Ma, W. Shang, W. Yu, X. Chen, W. Xia, C. Wang and P. Tan, *Energy Fuels*, 2021, **35**, 14188–14196.
44 G. He, L. Wang, H. Chen, X. Sun and X. Wang, *Mater. Lett.*, 2013, **98**, 164–167.
45 H. Wang, H. Dong, J. Lü, S. Sun, W. Zhang and S. Yao, *J. Electron. Mater.*, 2021, **50**, 4196–4206.
46 M. Karakoti, S. Pandey, G. Tatrari, P. S. Dhapola, R. Jangra, S. Dhali, M. Pathak, S. Mahendia and N. G. Sahoo, *Mater. Adv.*, 2022, **3**, 2146–2157.
47 C. Huang, Y. Ding, H. Chen, S. Zhou, X. Wang, H. Gao, L. Zhu and J. Wu, *Chem. Eng. J.*, 2019, **378**, 122202.
48 X. Chen and B. Chen, *Environ. Sci. Technol.*, 2015, **49**, 6181–6189.
49 C. Shan, H. Tang, T. Wong, L. He and S. Lee, *Adv. Mater.*, 2012, **24**, 2491–2495.
50 C. N. R. Rao, A. K. Sood, K. S. Subrahmanyam and A. Govindaraj, *Angew. Chem.*, 2009, **48**, 7752–7777.
51 L. Sun, H. Li, L. Ren and C. Hu, *Solid State Sci.*, 2009, **11**, 108–112.
52 X. He, S. Zhang, H. Pan, J. Chen and J. Xu, *Nanoscale Res. Lett.*, 2019, **14**, 117.
53 K. I. Nargatti, S. S. Ahankari, J. R. C. Dizon and R. Subramaniam, *ACS Omega*, 2024, **9**, 11730–11737.
54 X. Li, Z. Lu, S. Y. Chuah, W. Li, Y. Liu, W. Duan and Z. Li, *Composites, Part A*, 2017, **100**, 1–8.
55 S. Al-Rubaye, R. Rajagopalan, S. X. Dou and Z. Cheng, *J. Mater. Chem. A*, 2017, **5**, 18989–18997.
56 O. Okhay and A. Tkach, *Nanomaterials*, 2021, **11**, 1240.
57 A. Ambrosi, C. K. Chua, A. Bonanni and M. Pumera, *Chem. Rev.*, 2014, **114**, 7150–7188.
58 C. Li and G. Shi, *Nanoscale*, 2012, **4**, 5549.
59 S. Sun, S. Wang, S. Li, Y. Li, Y. Zhang, J. Chen, Z. Zhang, S. Fang and P. Wang, *J. Mater. Chem. A*, 2016, **4**, 18646–18653.
60 M. Srivastava, Md. E. Uddin, J. Singh, N. H. Kim and J. H. Lee, *J. Alloys Compd.*, 2014, **590**, 266–276.
61 Y. Su and A. Manthiram, *Nat. Commun.*, 2012, **3**, 1166.
62 C. Yuan, J. Li, L. Hou, X. Zhang, L. Shen and X. W. D. Lou, *Adv. Funct. Mater.*, 2012, **22**, 4592–4597.
63 E. Umeshbabu, G. Rajeshkhanna and G. R. Rao, *Int. J. Hydrogen Energy*, 2014, **39**, 15627–15638.
64 N. Sahoo, G. Tatrari, C. Tewari, M. Karakoti, B. S. Bohra and A. Dandapat, *RSC Adv.*, 2022, **12**, 5118–5134.
65 L. Zhao, H. Dai, F. Pei, P. Ming, X. Wei and J. Zhou, *Energies*, 2022, **15**, 386.
66 Z. Chen and N. Author_Id, *Int. J. Electrochem. Sci.*, 2021, **16**, 210914.
67 M. S. Rahmanifar, H. Hesari, A. Noori, M. Y. Masoomi, A. Morsali and M. F. Mousavi, *Electrochim. Acta*, 2018, **275**, 76–86.
68 Z. Cao, C. Liu, Y. Huang, Y. Gao, Y. Wang, Z. Li, Y. Yan and M. Zhang, *J. Power Sources*, 2020, **449**, 227571.
69 Y. Zhang, B. Wang, F. Liu, J. P. Cheng, X. Zhang and L. Zhang, *Nano Energy*, 2016, **27**, 627–637.
70 W. Liu, C. Lu, K. Liang and B. K. Tay, *J. Mater. Chem. A*, 2014, **2**, 5100–5107.
71 H. Jiang, K. Yang, P. Ye, Q. Huang, L. Wang and S. Li, *RSC Adv.*, 2018, **8**, 37550–37556.
72 S. Sun, S. Wang, S. Li, Y. Li, Y. Zhang, J. Chen, Z. Zhang, S. Fang and P. Wang, *J. Mater. Chem. A*, 2016, **4**, 18646–18653.